Thermophysical Property Matching and Numerical Simulation-Driven Design and Optimization of Hardfacing Layers on H13 Steel

Wenhao Yu1, Yanxiang Li1,2, Gang Liu3, Lin Yang4, Dongliang Li4, and *Xiang Chen1,2

School of Materials Science and Engineering, Tsinghua University, Beijing 100084, China
 Key Laboratory for Advanced Materials Processing Technology, Ministry of Education, Tsinghua University, Beijing 100084,
 China; 3. Zhejiang Tunnel Engineering Group Co., Ltd, Hangzhou 310005, Zhejiang, China; 4. Ningbo QingKe Laser Additive Manufacturing Technology Co., Ltd, Ningbo 315191, Zhejiang, China

*Corresponding address: e-mail: xchen@tsinghua.edu.cn

Abstract: A computational design methodology based on thermophysical property matching and numerical simulation is systematically studied in this paper to meet the demand for novel hardfacing materials in the surfacing repair of H13 tool steel. By integrating CALPHAD-based calculations with the dynamic time warping algorithm, a multi-parameter evaluation model was established to quantitatively characterize the thermophysical property mismatch between the substrate and filler material. Univariate sensitivity analysis and response surface methodology were employed to optimize the composition of filler material based on Caldie tool steel, identified as a promising candidate for hardfacing wires. Thermo-mechanical coupled numerical simulations were conducted to assess the stress distribution characteristics before and after composition optimization. The results indicate that through the coordinated adjustment of C, Si, and MC-type carbide-forming elements, the overall thermophysical property mismatch between the substrate and filler was reduced from 3.9 to below 0.4. Consequently, the distribution of equivalent plastic strain in the weld seam was improved, local stress concentrations were mitigated, and the average maximum principal stress was reduced by approximately 12%. These findings validate the reliability of the proposed thermophysical property matching evaluation method and provide a novel strategy for the design and optimization of hardfacing materials for tool steel repair.

Keywords: Hardfacing; H13 steel; Thermophysical property matching; Numerical simulation; Computational design methodology

1 Introduction

H13 steel is widely utilized high-temperature forming applications such as die casting and hot forging, owing to its excellent hardenability, high-temperature strength, wear resistance, and thermal fatigue resistance [1-4]. However, under cyclic mechanical stresses and impact loads, the surface of H13 molds is prone to progressive damage mechanisms including plastic deformation, wear, fatigue failure, and thermal cracking, which collectively diminish service lifetimes [5-8]. Hardfacing technology, as an economically viable remanufacturing strategy, offers a promising route to restore damaged surfaces or enhance localized properties through deposition of high-performance alloy layers [9-11], offering a promising solution to address surface degradation issues in H13 steel.

In recent years, extensive efforts have been made to explore surface hardfacing repair strategies for H13 steel. For instance, Wang et al. [12] designed a composite hardfacing structure comprising a substrate, an interlayer, and a wear-resistant layer based on the Fe–Cr binary phase diagram, achieving successful restoration of H13

steel mandrels via submerged arc welding. Zhang et al. [13] employed a compositional fine-tuning approach to develop a flux-cored wire with a Fe-0.5C-5.5Cr-1.5Mn-2.0W-1.0V composition, resulting in a sound metallurgical bonding interface. Nevertheless, two major challenges remain in the hardfacing-based remanufacturing of H13 steel: (i) the limited availability of filler wire types, which restricts the ability to tailor performance for varying service conditions; and (ii) the lack of fundamental understanding regarding the multiscale relationships between thermophysical property matching and the evolution of residual stresses.

Caldie tool steel, developed by Uddeholm, is a Cr-Mo-V alloyed tool steel that attains a hardness of up to 60 HRC after heat treatment and exhibits excellent resistance to adhesive wear and cracking [14,15], making it a highly promising candidate material for surface strengthening of similar alloy systems. Nevertheless, dissimilar material welding inherently risks interfacial incompatibility due to divergent thermophysical properties, particularly mismatches in coefficient of thermal expansion (CTE) and thermal conductivity (TC).

Such mismatches promote residual tensile stresses and cracking susceptibility during solidification and service [16-20] . Recent advances in numerical simulation techniques, particularly thermo-mechanical coupled finite element analysis (FEA), provide an efficient means for evaluating welding-induced stresses [21-24] . These approaches offer a pathway for the design and optimization of hardfacing layers and hold promise for the evaluation and development of novel materials for the surface repair of H13 steel.

In this study, a thermo-mechanical coupled finite element model for the hardfacing repair of H13 steel was established using the Simufact Welding simulation platform. An innovative approach was developed by integrating CALPHAD-based thermodynamic calculations with a dynamic curve similarity evaluation method to quantitatively assess the multi-parameter thermophysical property matching between substrate and filler materials. The composition of Caldie tool steel, identified as a promising candidate for hardfacing wire, was optimized using univariate sensitivity analysis and surface methodology response (RSM). Thermo-mechanical simulations were conducted to compare the stress distribution characteristics before and compositional refinement. The underlying relationship between thermophysical property matching and the evolution of welding-induced stresses was clarified, thereby establishing a numerically driven design paradigm for hardfacing material development in H13 steel hardfacing repair.

2 Finite element model

2.1 Geometrical model and mesh generation

Based on the actual hardfacing conditions, the finite element model consisted of a supporting platform ($140 \times 120 \times 20$ mm), a substrate ($100 \times 80 \times 20$ mm), and five parallel, unidirectional weld beads ($100 \times 12 \times 3$ mm). Structured hexahedral elements were uniformly applied across all components to ensure numerical stability during thermo-mechanical coupled analyses, resulting in a total of 61,500 mesh elements.

2.2 Heat source model

The ellipsoidal heat source model proposed by Goldak et al. has been widely applied in welding and additive manufacturing processes [25–27]. A schematic illustration of the double-ellipsoidal heat source model is shown in **Fig. 2**. In this model, the front semi-axis length was set to 4.0 mm, the rear semi-axis length to 15.0 mm, the width to 8.0 mm, and the depth to 8.0 mm.

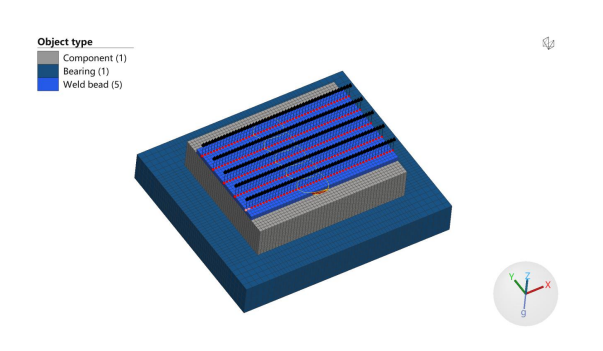


Fig. 1. Geometrical model and mesh generation for finite element analysis.

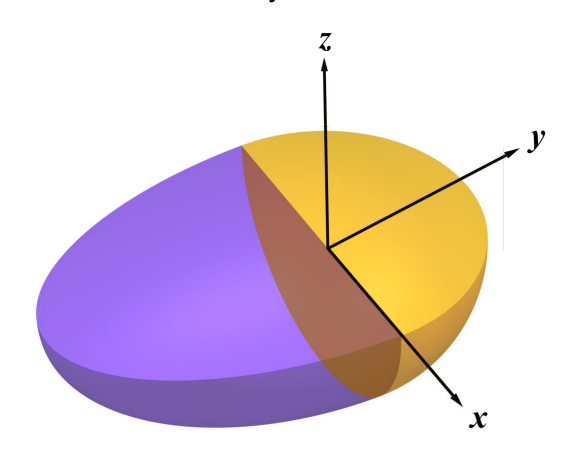


Fig. 2. Schematic diagram of the double-ellipsoidal heat source

2.3 Material model

The substrate and hardfacing layer were modeled as H13 hot-work tool steel and Caldie tool steel, respectively, with their full chemical composition detailed Table 1. To incorporate temperature-dependent evolution of thermomechanical properties throughout the welding thermal cycle, thermophysical parameters of the substrate and hardfacing layer were calculated using JMatPro 7.0 software based on the CALPHAD methodology. The calculated results for the coefficients of thermal expansion, thermal conductivity, Young's modulus, and specific heat capacity are shown in Fig. 3.

2.4 Process parameters

The welding process parameters were defined to simulate the industrial hardfacing conditions. The substrate preheating temperature was maintained at 300°C. In addition, the welding voltage and current were set to 22 V and 220 A, respectively, with a travel speed of 200 mm/min. An interpass dwell time of 100 s was applied to mitigate the risk of overheating caused by continuous heat input.

	С	Cr	Mn	Mo	V	Si	Fe
Substrate-H13	0.4	5.0	0.4	1.4	1.0	1.0	Bal.
Hardfacing layer-Caldie	0.7	5.0	0.5	2.3	0.5	0.2	Bal.

Table 1. Chemical compositions of substrate and hardfacing layer (wt.%)

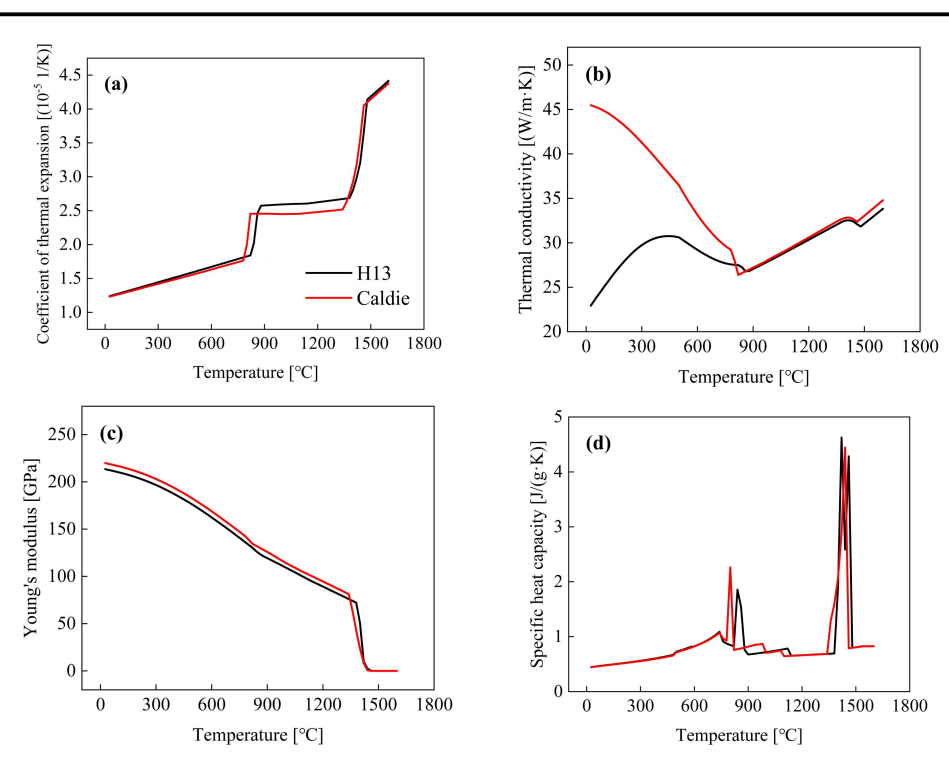


Fig. 3. Thermophysical properties of the substrate and hardfacing layer: (a) Coefficient of thermal expansion; (b) Thermal conductivity; (c)

Young's modulus; (d) Specific heat capacity.

3 Results and discussion

3.1 Development of a thermophysical property matching metrics

As evidenced in Fig. 3, significant thermophysical property disparities exist between the H13 substrate and Caldie hardfacing layer, most notably in thermal conductivity. During the cooling stage (particularly below 900°C), divergent thermal conductivities mismatched heat dissipation rates, generating steep thermal gradients across the interfacial region. These gradients drive heterogeneous contraction behavior, thereby amplifying thermal stress accumulation. To address this intrinsic incompatibility, compositional optimization of the Caldie filler material was pursued to enhance thermophysical congruence with the substrate. To achieve precise compositional adjustments, a quantitative evaluation index must be established to systematically assess the degree of thermophysical property matching.

Several methods are available for evaluating curve

similarity, including Euclidean distance, correlation coefficient, and dynamic time warping (DTW) [28-30]. Among these, the Euclidean distance method requires However. strict alignment of the curves. thermophysical property curves (e.g., conductivity) of the substrate and hardfacing layer often exhibit asynchronous variations along the temperature axis, making Euclidean distance prone to misjudging key features such as inflection points and peaks due to phase differences. The correlation coefficient method reflects only linear relationships and fails to quantify differences in curve morphology. DTW, by contrast, is a nonlinear time-series alignment algorithm that employs dynamic programming to identify the optimal matching path between two curves while minimizing cumulative distance. DTW allows for local stretching compression along the temperature axis, thus overcoming the strict alignment limitations of traditional methods. The calculation procedure for the thermophysical property matching metric is outlined as follows:

(1) Parameter definitions

The substrate and hardfacing layer materials are denoted as B and H, respectively. Their sets of thermophysical properties are defined as:

$$P = \{CTE, TC, YM, SHC\}$$
 (1)

where CTE, TC, YM, and SHC represent the coefficient of thermal expansion, thermal conductivity, Young's modulus, and specific heat capacity, respectively.

The temperature sequence is given by:

$$T = [T_1, T_2, ..., T_N] (2)$$

where N is the number of temperature sampling points, covering the range from 1600 °C down to room temperature with a 20°C sampling interval.

The thermophysical property data matrices for the substrate and hardfacing layer are defined as:

$$X_p^{(B)} = \left[x_{p,1}^{(B)}, ..., x_{p,N}^{(B)} \right]$$
 (3)

$$X_p^{(H)} = \left[x_{p,1}^{(H)}, ..., x_{p,N}^{(H)} \right] \tag{4}$$

where $p \in P$, and $x_{p,i}$ represents the value of property p at the i-th temperature point.

(2) Global normalization

For each property p, the global minimum and maximum values across all materials (including both the substrate and the hardfacing layer) are calculated as:

$$x_{p,min} = min \left(\bigcup_{M \in \{B,H\}} X_p^{(M)} \right) \tag{5}$$

$$x_{p,max} = \max\left(\bigcup_{M \in \{B,H\}} X_p^{(M)}\right) \tag{6}$$

Global normalization is applied to eliminate the influence of differing units among properties. The normalized sequence is expressed as:

$$\widetilde{X_{p}^{(M)}} = \left[\frac{x_{p,1}^{(M)} - x_{p,min}}{x_{p,max} - x_{p,min}}, ..., \frac{x_{p,N}^{(M)} - x_{p,min}}{x_{p,max} - x_{p,min}} \right]$$
(7)

(3) DTW distance calculation

For each property p, compute pairwise deviations between normalized substrate and hardfacing profiles. The local distance matrix is computed as:

$$C(i,j) = \left| \widetilde{X_{p,i}^{(B)}} - \widetilde{X_{p,j}^{(H)}} \right| \ \forall i,j \in \{1,...,N\}$$
 (8)

Then, the cumulative distance matrix is obtained by dynamic programming recursion:

$$D(i,j) = C(i,j) + min \begin{cases} D(i-1,j) \\ D(i,j-1) \\ D(i-1,j-1) \end{cases}$$
(9)

Initialize boundary conditions:

$$D(1,1) = C(1,1) \tag{10}$$

$$D(i,1) = D(i-1,1) + C(i,1)$$
(11)

$$D(1,j) = D(1,j-1) + C(1,j)$$
(12)

The DTW distance (minimal cumulative distance) for property p is defined as:

$$D_p = D(N, N) = \min_{\pi \in \Pi} \sum_{(i,j) \in \pi} C(i,j)$$
(13)

where Π represents the set of all warping paths satisfying the endpoint alignment and monotonic continuity constraints.

Based on the above derivation, the overall thermophysical property matching degree between the substrate and the hardfacing layer is calculated as:

$$D_{Total} = \sum w_p D_p \ \forall p \in P \tag{14}$$

 $D_{Total} = \sum_{P \in P} w_p D_p \ \forall p \in P$ (14) where P_p^{P} is the weight assigned to each property. In this study, equal weighting was applied to the four thermophysical properties, with $w_p = 0.25$ for all p. It can thus be inferred that a smaller D_{Total} value indicates a higher degree of similarity between the property curves, improved thermophysical corresponding to an compatibility between the substrate and the hardfacing layer.

3.2 Composition optimization of welding wire based on thermophysical property matching

Based on the computational framework established in Section 3.1, the individual and overall thermophysical property mismatching degrees between Caldie steel and H13 steel were calculated, as summarized in Table 2. It can be observed that the thermal conductivity exhibited the largest calculated mismatch value, indicating a significant discrepancy in this property. This result is consistent with the trend shown in Fig. 3 and further validates the reliability of the proposed thermophysical property matching metric.

Table 2. Individual and overall thermophysical property mismatching degrees between Caldie and H13 steel.

D_{CTE}	D_{TC}	D_{YM}	D_{SHC}	D_{Total}	
0.8	13.4	0.5	0.7	3.9	

To address the thermophysical mismatch between Caldie and H13 steel, enhance the weldability of the hardfacing layer, concurrently preserve its and mechanical performance, the chemical composition of Caldie steel was optimized based on CALPHAD calculations and fundamental metallurgical principles.

3.2.1 Carbon content optimization

The mass fraction of carbon (C) in Caldie steel is as high as 0.7%. However, an excessive C content significantly increases the susceptibility to welding hot cracking [31]. Therefore, it is necessary to appropriately reduce the C equivalent to improve weldability. As

shown in **Fig. 4**, the thermophysical properties of Caldie steel with varying C contents (0.4–0.7%) were calculated using the CALPHAD approach. The corresponding influence of C content on the thermophysical property mismatching between Caldie and H13 steel is illustrated in **Fig. 5**. It is evident that the thermophysical mismatch is primarily governed by thermal conductivity; as the C content decreases, both the thermal conductivity and the overall property matching improve. However, an excessively low C content would significantly compromise the hardness and wear resistance of the

hardfacing layer. Therefore, considering the trade-off between weldability and wear resistance, the C content was reduced to 0.5% in this study. To compensate for the potential loss in hardness, elements such as V, Ti, and Nb were introduced to enhance fine-grain strengthening and carbide dispersion strengthening, synergized with the solid solution strengthening effect of Si. Following the C adjustment, the overall thermophysical mismatch between the substrate and the hardfacing layer decreased from 3.9 to 3.0.

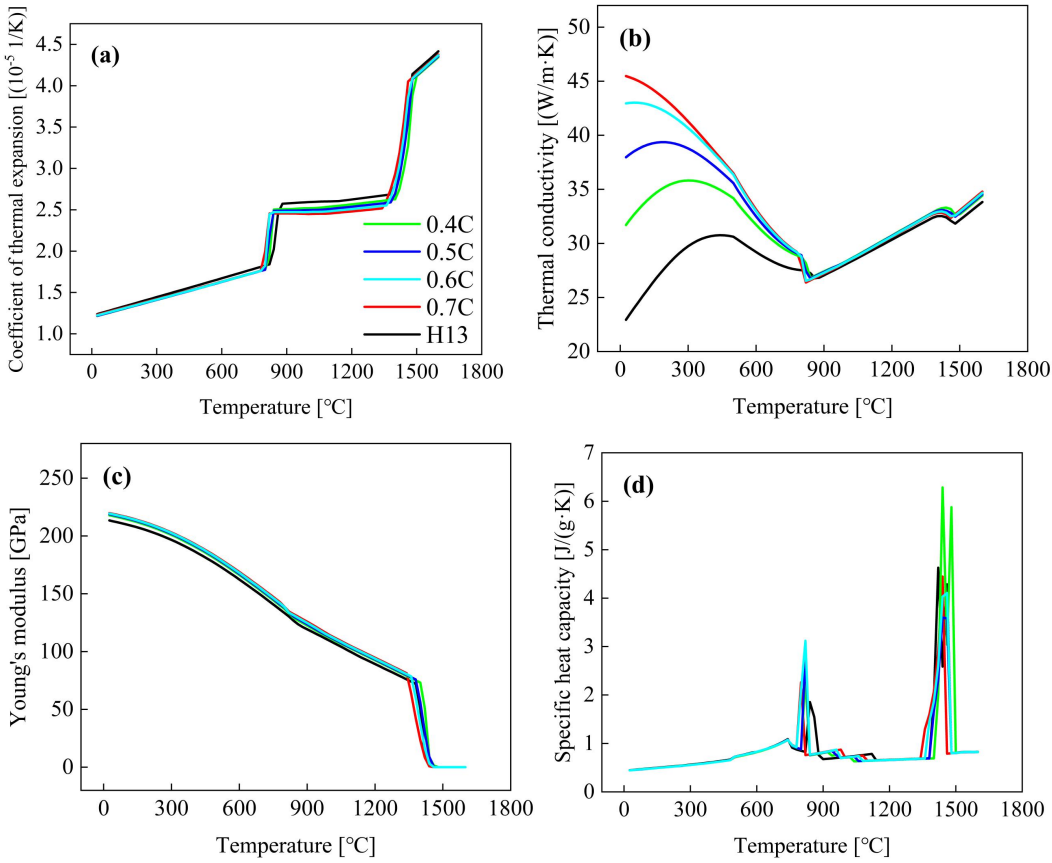


Fig. 4. C content-dependent thermomechanical properties of Caldie tool steel: (a) CTE; (b) TC; (c) YM; (d) SHC.

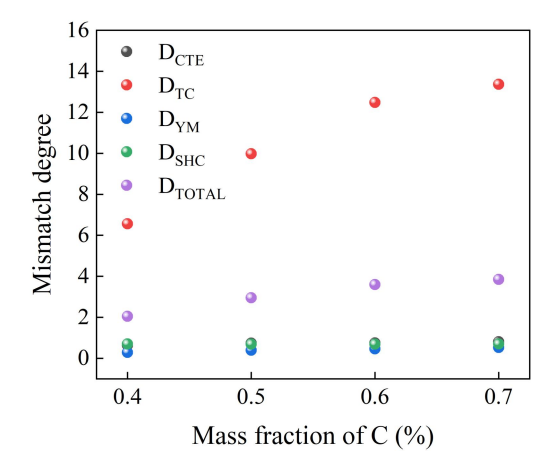


Fig. 5. Influence of C content on thermophysical compatibility metrics between Caldie and H13 Steel.

3.2.2 Silicon content optimization

Silicon (Si) is a commonly used deoxidizer in welding metallurgy, capable of reducing the oxygen content in the molten pool and minimizing the formation of pores and inclusions. As shown in **Fig. 6** and **Fig. 7**, the overall thermophysical property mismatch degree decreases with increasing Si content, indicating an improvement in matching between the substrate and the hardfacing layer. However, an excessive Si addition may compromise the toughness of the weld metal. Therefore, in this study, the Si content was moderately increased to 0.6%. Following the adjustment of the Si content, the overall thermophysical mismatch between the substrate and the hardfacing layer was further reduced to 2.0.

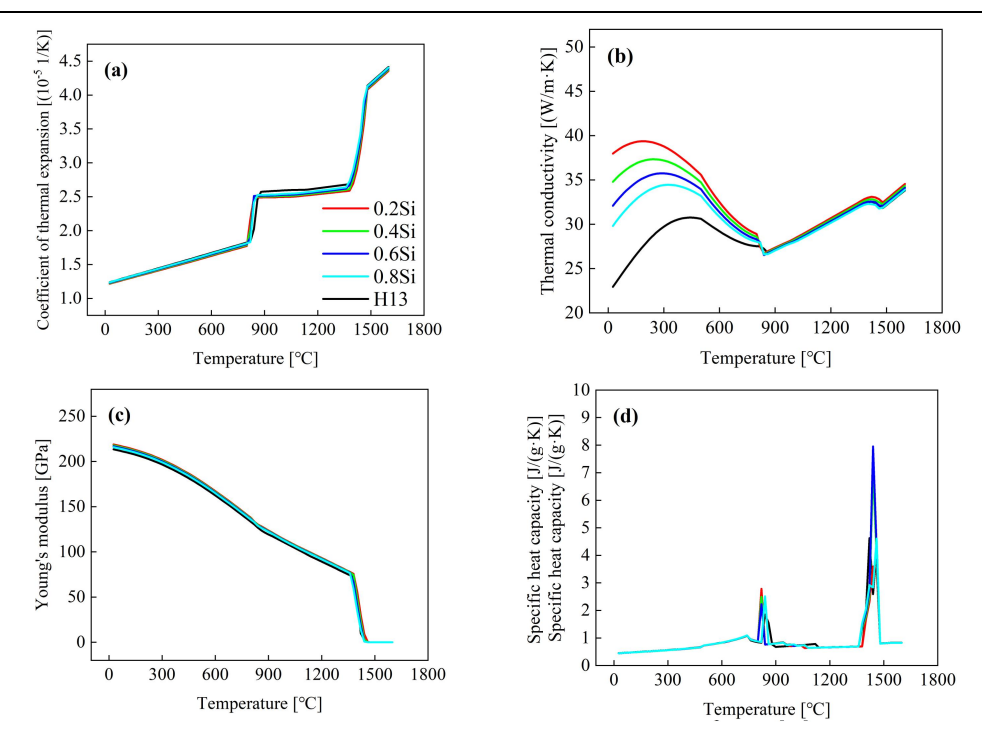


Fig. 6. Influence of Si content on thermophysical properties of Fe-0.5C-5Cr-0.5Mn-2.3Mo-0.5V-xSi Alloy: (a) CTE; (b) TC; (c) YM; (d) SHC.

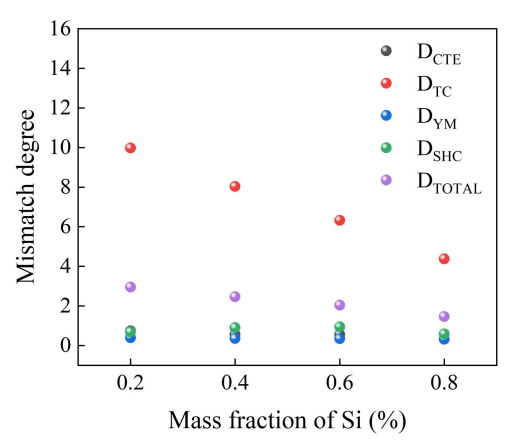


Fig. 7. Effects of Si content on thermophysical compatibility metrics between Fe-0.5C-5Cr-0.5Mn-2.3Mo-0.5V-xSi and H13 steel 3.2.3 Synergistic optimization of MC-type carbide-forming elements

Vanadium (V), niobium (Nb), and titanium (Ti) are typical MC-type carbide-forming elements, where the formation of high-hardness MC-type carbides can effectively pin austenite grain boundaries and suppress grain coarsening. However, excessive addition of a single carbide-forming element may lead to particle agglomeration, resulting in reduced toughness and increased susceptibility to cracking [32,33]. Previous studies have indicated that the synergistic addition of V, Nb, and Ti promotes the formation of heterogeneous

nucleation sites, facilitating the precipitation of fine, uniformly distributed composite carbides with enhanced mechanical properties [34,35]. Therefore, the RSM was employed to investigate the effect of Nb and Ti contents on the thermophysical property matching degree under different V contents (0.5%, 1.0%, 1.5%, and 2.0%). Considering the cost constraint, the Nb and Ti contents were limited to below 0.6%. The results are presented in **Fig. 8**. It can be observed that when the V, Nb, and Ti contents are optimized to 1.0%, 0.6%, and 0.2%, respectively, the overall thermophysical property mismatch between the substrate and the hardfacing layer is minimized to below 0.4.

In summary, based on the concept of thermophysical property matching and considering the weldability requirements, the optimized hardfacing composition was determined to be Fe-0.5C-5.0Cr-0.5Mn-2.3Mo-1.0V-0.6Si-0.6Nb-0.2Ti. CALPHAD-predicted thermophysical properties of the baseline Caldie, optimized Caldie, and H13 substrate are comparatively analyzed in Fig. 9. It can be observed that, overall, the optimized hardfacing material exhibits significantly improved thermophysical compatibility with the substrate.

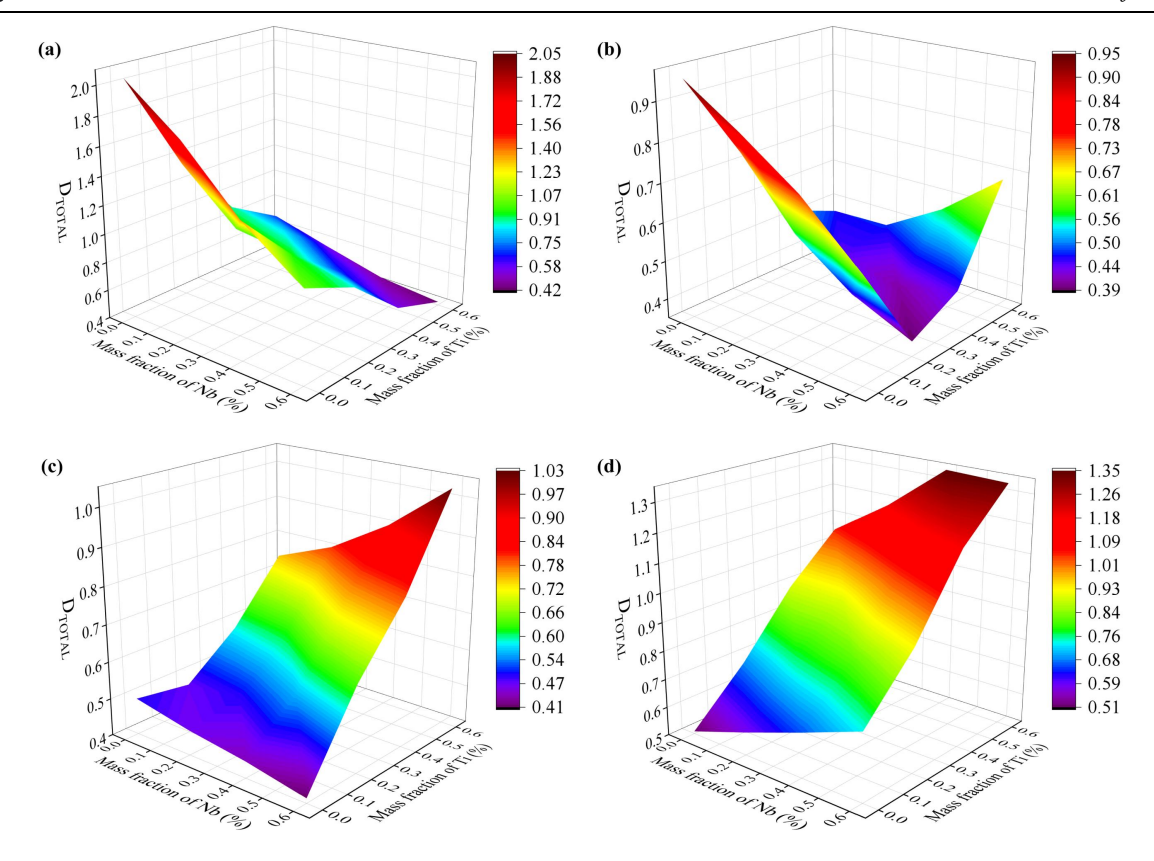


Fig. 8. Effect of Nb-Ti synergistic interactions on thermophysical compatibility across varied V contents: (a) V = 0.5 wt.%; (b) V = 1.0 wt.%; (c) V = 1.5 wt.%; (d) V = 2.0 wt.%.

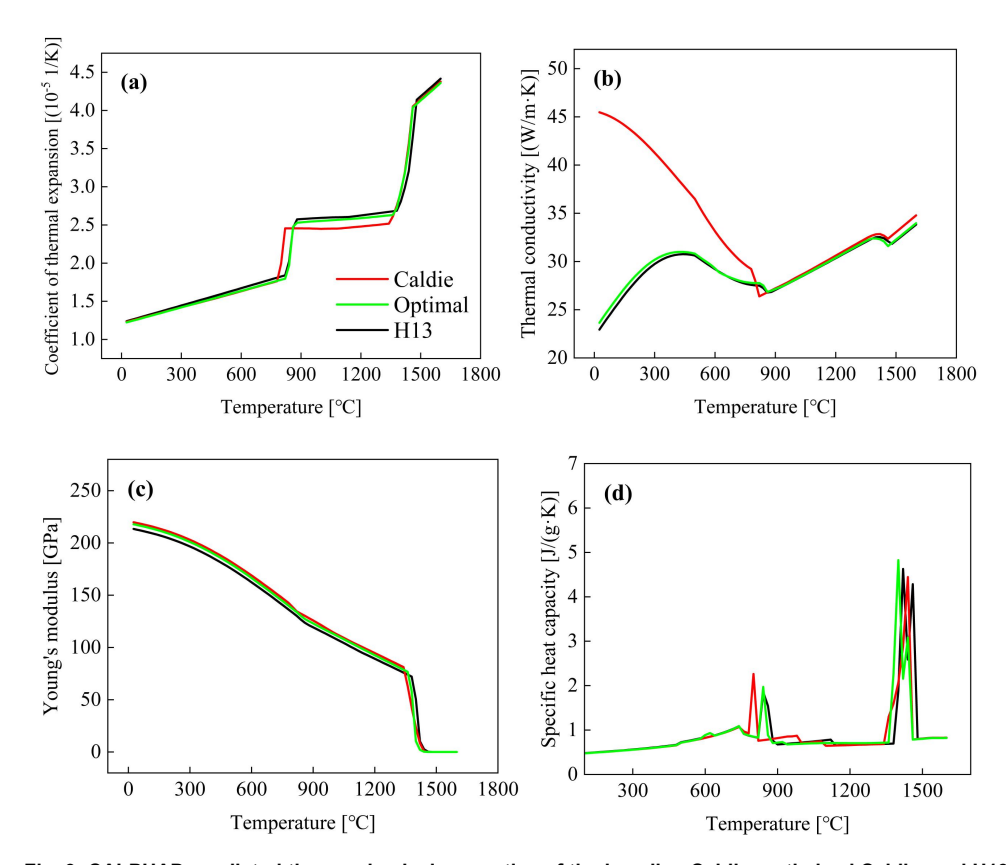


Fig. 9. CALPHAD-predicted thermophysical properties of the baseline Caldie, optimized Caldie, and H13 substrate: (a) CTE; (b) TC; (c) YM; (d) SHC.

3.3 Comparison of numerical simulation results

To evaluate the effectiveness of the hardfacing alloy optimization in regulating welding residual stresses, a numerical simulation approach was employed to establish a correlation model between filler metal composition and thermal stress response. The stress distribution characteristics of baseline and optimized hardfacing wires were systematically compared across critical deposition stages: (i) post-initial pass cooling phase (Stage I) and (ii) subsequent pass thermal cycles (Stage II).

3.3.1 Post-cooling analysis of initial weld pass (Stage I)

Fig. 10 presents the overall contour maps and X-axis sectional profiles of the first principal stress (σ_1) after the cooling of the first weld pass and before the initiation of the second weld pass, using both the original

and optimized Caldie compositions as the hardfacing material. The results indicate that the stress distribution characteristics are similar for both cases: stresses are primarily concentrated in the heat-affected zone (HAZ) of the substrate, the central portion of the weld seam offset toward the positive Y-direction (adjacent to the unwelded region), and at the interface between the substrate and the weld metal. The overall stress ranges are nearly identical, spanning -73 MPa to 698 MPa before optimization and -72 MPa to 703 MPa after optimization, with the peak stress located in the substrate's HAZ in both scenarios. These results suggest that the optimization of the filler composition has minimal influence on the stress distribution within the substrate's HAZ.

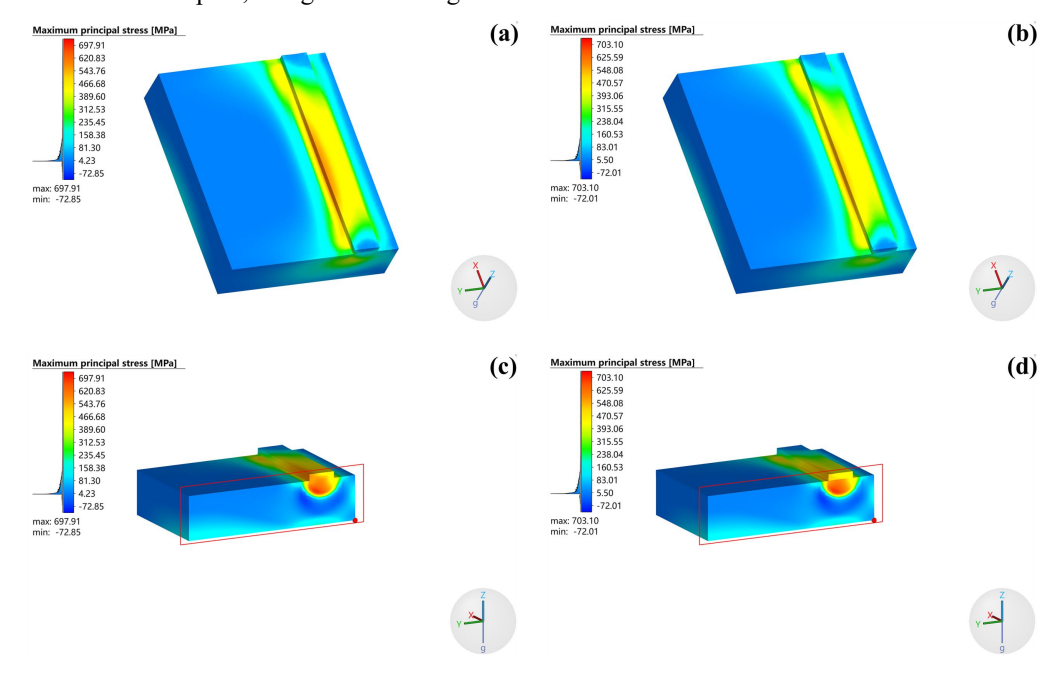


Fig. 10. First principal stress distribution comparison: (a-b) full-field contours; (c-d) X-axis cross-sectional profiles.

However, notable differences arise between the two cases in terms of stress distribution and peak stress within the weld seam itself. **Fig. 11** displays the stress distribution localized in the weld seam after cooling of the first pass and prior to deposition of the second pass. It can be seen that, after compositional optimization, the maximum σ_1 value in the weld decreases from 604 MPa to 556 MPa. To better visualize the evolution of stress distribution characteristics, a unified color scale was

adopted, focusing specifically on regions where σ_1 exceeds 500 MPa, as shown in **Fig. 12**. The results demonstrate that the optimized filler composition leads to a notable reduction in the proportion of high-stress areas. This trend is further confirmed by the corresponding stress density plots in the legends, highlighting a decrease in the extent and intensity of the high-stress zones when using the optimized composition.

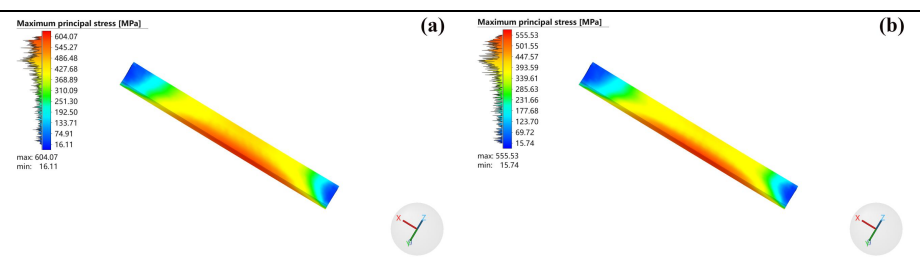


Fig. 11. Comparative first principal stress distribution within the weld zone after initial pass cooling:

(a) baseline composition; (b) optimized composition.

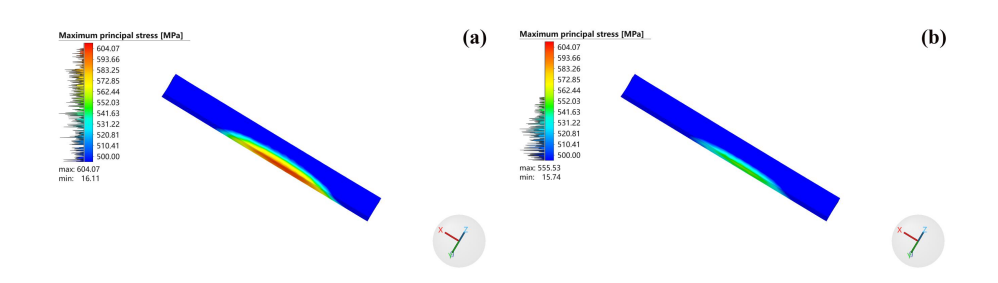


Fig. 12. Unified-scale comparison of first principal stress distribution within the weld zone after initial pass cooling:

(a) baseline composition; (b) optimized composition.

As shown in **Fig. 9**(b), the optimized composition exhibits a lower thermal conductivity compared to the original Caldie steel in the medium and low temperature range (below 900 °C). This reduction in thermal conductivity effectively prolongs the cooling time within this temperature regime, thereby providing a more favorable window for stress relaxation in the deposited layer. Furthermore, **Fig. 9**(c) reveals a decrease in Young's modulus for the optimized composition, which facilitates the accumulation of plastic strain within the weld deposit, enabling greater stress relief through enhanced plastic deformation. This interpretation is substantiated by the equivalent plastic strain contour maps presented in **Fig. 13**. A comparison of the legends

indicates that when using the original Caldie composition, the equivalent plastic strain is predominantly distributed below 0.05, with a maximum value of 0.09. In contrast, for the optimized composition, the principal distribution range extends up to 0.06, with a slightly increased maximum value of 0.10. Moreover, in the case of Caldie, plastic strain is highly localized near the weld centerline, indicating a predominance of elastic behavior in the majority of the weld (evidenced by the extensive blue regions). Conversely, with the optimized composition, the proportion of high strain regions (green zones) increases and spreads toward the high stress side, as shown in **Fig. 10**, thereby effectively mitigating local stress concentrations.

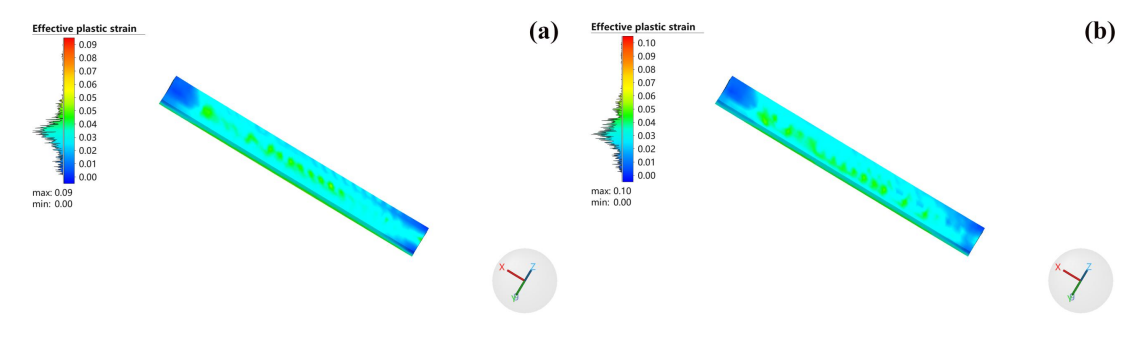


Fig. 13. Comparison of equivalent plastic strain distributions in the weld seam after cooling of the first weld pass: (a) before optimization; (b) after optimization.

3.3.2 Cooling process following subsequent weld passes (Stage II)

As illustrated in Fig. 14, the distributions of the first

principal stress σ_1 after the cooling of subsequent weld passes (from the second to the fifth pass) were analyzed for both the original and optimized filler compositions.

Overall, regardless of composition optimization, the maximum σ_1 within the weld seam exhibited a decreasing trend with the addition of subsequent passes, primarily due to tempering effects induced by thermal cycling. Furthermore, high stress regions, initially concentrated at the edges of the newly deposited welds, progressively extended towards the interfaces between successive weld passes. Correspondingly, a comparative

analysis of the maximum σ_1 values for each pass before and after filler composition optimization is presented in Fig. 15. It is evident that the optimized composition effectively mitigates the risk of high stress within the weld seam, achieving an average reduction of approximately 12%. The underlying mechanisms are consistent with the phenomena discussed previously in Section 3.3.1.

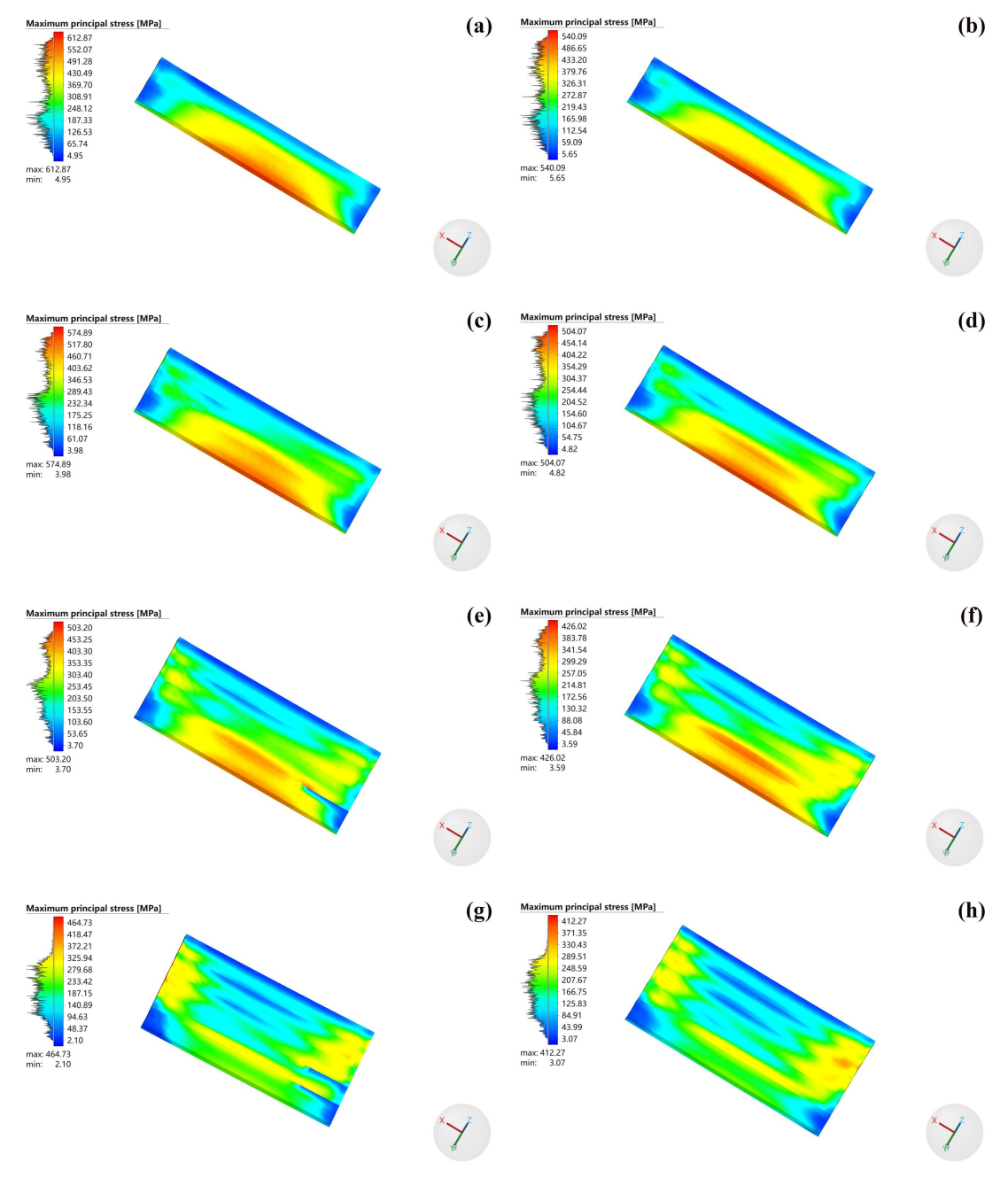


Fig. 14. Distribution maps of the first principal stress after cooling of subsequent weld passes (numbers indicate the pass sequence; C and O denote Caldie and optimized Caldie, respectively): (a) 2-C; (b) 2-O; (c) 3-C; (d) 3-O; (e) 4-C; (f) 4-O; (g) 5-C; (h) 5-O.

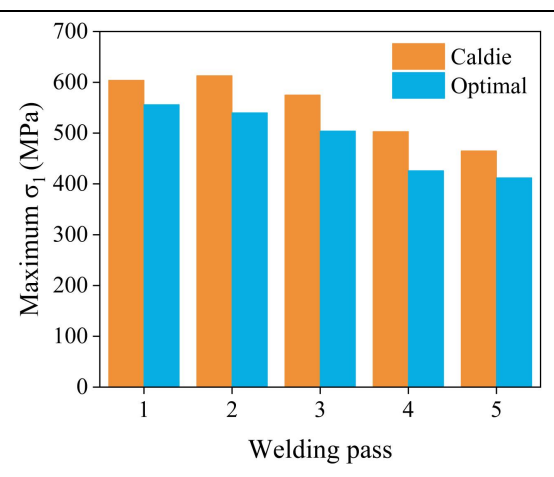


Fig. 15. Comparative analysis of peak first principal stress magnitudes between Caldie and optimized Caldie across multipass deposition.

However, it is noteworthy that for the original Caldie weld wire, the first principal stress after cooling of the second weld pass exhibits an anomalous increase compared to the first pass, in stark contrast to the continuous decreasing trend observed in the optimized wire. This phenomenon was further investigated by examining the distribution characteristics of the equivalent plastic strain after cooling of the second pass. As shown in **Fig. 16**, the second pass welded with the original Caldie wire displays pronounced localized plastic strain after cooling, characterized by a narrow yellow band (strain > 0.05) aligned along the weld centerline, accompanied by steep strain gradients on either side. This indicates highly localized plastic deformation with insufficient energy dissipation, with the

peak equivalent plastic strain reaching 0.09. By contrast, for the optimized Caldie composition, the peak equivalent plastic strain after the second pass increases slightly to 0.10, and the high strain regions extend toward the weld edges and the interface between the new and previous welds. This distribution characteristic is attributed to the synergistic optimization of thermal conductivity and Young's modulus: the reduced thermal conductivity at intermediate temperatures prolongs the time window for plastic deformation, while the decreased modulus promotes strain accommodation across the new and previous weld interfaces, thereby effectively suppressing the anomalous rise in residual stress following the second pass.

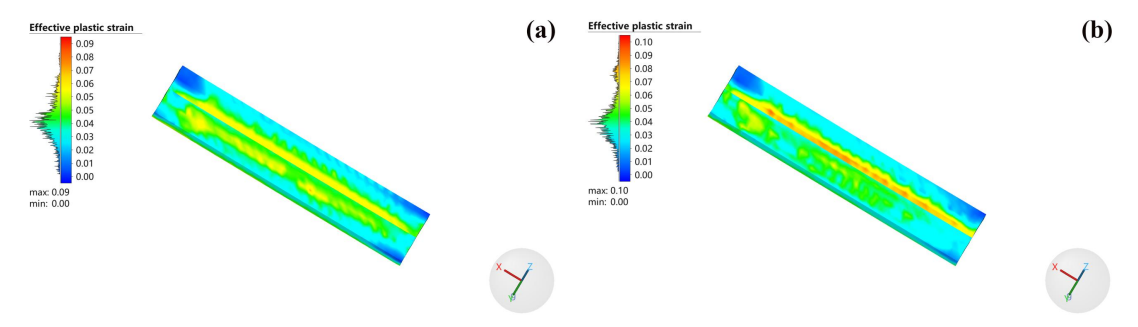


Fig. 16. Comparison of equivalent plastic strain distribution after cooling of the second weld pass:

(a) before optimization; (b) after optimization.

4 Conclusions

1. By integrating CALPHAD thermodynamic calculations with the dynamic time warping (DTW) algorithm, a multi-parametric compatibility index was established to evaluate synergistic matches across critical properties, including coefficients of thermal expansion, thermal conductivity, Young's modulus, and specific heat capacity. This framework enables quantitative assessment of thermophysical disparities between base materials and filler alloys.

- 2. Through the integration of univariate sensitivity analysis and response surface methodology, the chemical composition of Caldie tool steel was systematically optimized for hardfacing applications on H13 steel. By means of the synergistic adjustment of C, Si, V, Nb, and Ti, the overall thermophysical mismatch degree was reduced from 3.9 to below 0.4.
- 3. The tailored thermophysical compatibility significantly improved the distribution of equivalent plastic strain within the weld deposit, mitigated local

stress concentrations, and achieved an average reduction of approximately 12% in the peak first principal stress. These findings validate the efficacy of the proposed matching metric and introduce a novel methodological framework for the development of hardfacing repair materials.

Acknowledgments

This work was supported by the Inner Mongolia Key Research and Development and Achievement Transformation Plan Project (No. 2023YFJM0004).

Conflicts of interest

The authors declare that they have no known competing financial interests or personal relationships that could have appeared to influence the work reported in this paper.

References

- [1] X. Du, X. Liu, Y. Shen, R. Liu, Y. Wei, H13 tool steel fabricated by wire arc additive manufacturing: Solidification mode, microstructure evolution mechanism and mechanical properties, Materials Science and Engineering: A 883 (2023) 145536.
- [2] J. Luo, J. Wang, J. Xu, Effect of laser shock peening on plasma nitriding microstructure and properties of H13 steel, Surf Coat Technol 473 (2023) 130004.
- [3] S.S. Joshi, S. Sharma, S. Mazumder, M. V Pantawane, N.B. Dahotre, Solidification and microstructure evolution in additively manufactured H13 steel via directed energy deposition: Integrated experimental and computational approach, J Manuf Process 68 (2021) 852–866.
- [4] G. Zhao, X. Zang, W. Li, Z. Zhao, D. Li, Study on primary carbides precipitation in H13 tool steel regarding cooling rate during solidification, China Foundry 17 (2020) 235–244.
- [5] Y. Li, X. Chen, S. Liu, W. Rao, Y. Li, Z. Xu, Q. Jiang, W. Liu, H. Liu, D. Liu, Study on the heterogeneous layer of H13 steel induced by ultrasonic surface rolling and the enhancement effect on its wear resistance, Journal of Materials Research and Technology 35 (2025) 7346–7361.
- [6] H. Chen, Y. Lu, Y. Sun, Y. Wei, X. Wang, D. Liu, Coarse TiC particles reinforced H13 steel matrix composites produced by laser cladding, Surf Coat Technol 395 (2020) 125867.
- [7] Z. Yang, C. Yan, J. Wang, T. Tang, P. Li, Z. Li, Investigation of failure analysis and failure delay strategy for H13 steel contact wire clip die, Eng Fail Anal 169 (2025) 109138.
- [8] B. Wu, M. Liu, G. Xu, Y. Zhu, J. Li, X. Wu, Fatigue damage and life prediction for AISI H13 steel under cyclic thermomechanical loading, Int J Fatigue 192 (2025) 108718.
- [9] M. Zhang, Z. Zhang, L. Lei, W. Zhou, M. Du, B. Zhang,

- Effect of repair weld length on microstructure evolution and mechanical properties of 30CrMnSiNi2A ultra-high strength steel, Journal of Materials Research and Technology 23 (2023) 4828–4842.
- [10] M. Attalla, S. Kandil, M.A.-H. Gepreel, M.A. Daha, Effect of employing buffer layer in repaired dissimilar welded joints on the residual stresses based on contour and slitting methods, J Manuf Process 73 (2022) 454–462.
- [11] P. Muangjunburee, H.Z. Oo, S.Z.A. Rahim, B. Srikarun, Abrasive wear performance of repair welds on R260 rail using different welding electrodes, Results in Engineering 26 (2025) 104680.
- [12] X. Wang, J. Wang, Z. Gao, D.-H. Xia, W. Hu, Fabrication of graded surfacing layer for the repair of failed H13 mandrel using submerged arc welding technology, J Mater Process Technol 262 (2018) 182–188.
- [13] M. Zhang, S. He, B. Jiang, X. Yao, K. Zhang, The Study on Feasibility and Welding Characteristics of GMAW Surfacing Remanufacturing of H13 Steel Cutter Ring of TBM Hob, Coatings 11 (2021).
- [14] UDDEHOLM CALDIE: High-Carbon, Chromium-Molybdenum-Vanadium Alloy Cold-Work Tool Steel, Alloy Digest 69 (2020) TS-785.
- [15] H. Li, X. Wu, G. Li, D. Zhou, Chipping damage of die for trimming advanced high-strength steel sheet: Evaluation and analysis, J Mater Process Technol 285 (2020) 116787.
- [16] N. Alcantar-Modragón, V. García-García, F. Reyes-Calderón, J.C. Villalobos-Brito, H.J. Vergara-Hernández, Study of cracking susceptibility in similar and dissimilar welds between carbon steel and austenitic stainless steel through finger test and FE numerical model, The International Journal of Advanced Manufacturing Technology 116 (2021) 2661–2686.
- [17] Y. Han, J. Chu, Q. Wang, K. Fu, H. Jin, Y. Wei, Investigation of microstructure, mechanical properties, residual stress, and distortion in multi-pass gas metal arc welding of ZGMn13Mo/A514 dissimilar joints, Mater Chem Phys (2025) 130941.
- [18] E.M. Anawa, A.G. Olabi, Control of welding residual stress for dissimilar laser welded materials, J Mater Process Technol 204 (2008) 22–33.
- [19] S. Carone, V. Moramarco, G. Pappalettera, G. Barbieri, C. Casavola, Residual stress measurement on Titanium Grade 5 and Inconel 625 thin dissimilar welded joints by contour method, J Mater Sci 57 (2022) 671–686.
- [20] H. Eisazadeh, A. Achuthan, J.A. Goldak, D.K. Aidun, Effect of material properties and mechanical tensioning load on residual stress formation in GTA 304-A36 dissimilar weld, J Mater Process Technol 222 (2015) 344-355.

- [21] C. Liu, H. Gao, L. Li, J. Wang, C. Guo, F. Jiang, A review on metal additive manufacturing: modeling and application of numerical simulation for heat and mass transfer and microstructure evolution, China Foundry 18 (2021) 317–334.
- [22] K. Zhang, S. Dai, B. Jiang, D. Wang, C. Han, Q. Liu, Simulation optimization and experimental research on heat-treatment process for ring remanufacturing of TBM disc cutters, Surf Coat Technol 475 (2023) 130133.
- [23] F. Jin, J. Li, Y. Du, X. Nan, J. Shi, J. Xiong, F. Zhang, Numerical simulation based upon friction coefficient model on thermo-mechanical coupling in rotary friction welding corresponding with corona-bond evolution, J Manuf Process 45 (2019) 595–602.
- [24] X. Shan, C.M. Davies, T. Wangsdan, N.P. O'Dowd, K.M. Nikbin, Thermo-mechanical modelling of a single-bead-on-plate weld using the finite element method, International Journal of Pressure Vessels and Piping 86 (2009) 110–121.
- [25] J. Goldak, A. Chakravarti, M. Bibby, A new finite element model for welding heat sources, Metallurgical Transactions B 15 (1984) 299–305.
- [26] S. Joshi, J. Hildebrand, A.S. Aloraier, T. Rabczuk, Characterization of material properties and heat source parameters in welding simulation of two overlapping beads on a substrate plate, Comput Mater Sci 69 (2013) 559–565.
- [27] X. Bai, P. Colegrove, J. Ding, X. Zhou, C. Diao, P. Bridgeman, J. roman Hönnige, H. Zhang, S. Williams, Numerical analysis of heat transfer and fluid flow in multilayer deposition of PAW-based wire and arc additive manufacturing, Int J Heat Mass Transf 124 (2018) 504–516.
- [28] H. Meng, R. Yu, Z. Tang, Z. Wen, H. Yu, Y. Chu, Formation ability descriptors for high-entropy diborides established through high-throughput experiments and

- machine learning, Acta Mater 256 (2023) 119132.
- [29] X. Ning, K. Zhu, Y. Deng, R. Zhang, Q. Chen, Z. Li, A New Similarity Measurement Method for the Power Load Curves Analysis, in: M. Cheng, P. Yu, Y. Hong, H. Jia (Eds.), Smart Grid and Innovative Frontiers in Telecommunications, Springer International Publishing, Cham, 2021: pp. 3–13.
- [30] M. Braig, P. Zeiler, A Study on the Effectiveness of Time Series Similarity Measures for the Comparison of Degradation Curves of Similar Engineering Systems, IEEE Access 12 (2024) 49602–49623.
- [31] K. Tamaki, K. H, J. and Suzuki, Effects of carbon content and peritectic reaction on hot cracking of high-carbon steel weld metal, Welding International 17 (2003) 26–35.
- [32] Z. Zhang, H. Liu, C. Yang, Z. Zhang, X. Chu, Y. Luan, X. Li, L. Hao, X. Zhang, Influence of microalloying element vanadium on microstructure and mechanical properties of anchor steel, Journal of Iron and Steel Research International (2024).
- [33] X. Li, Z. Cai, M. Hu, K. Li, M. Hou, J. Pan, Effect of NbC precipitation on toughness of X12CrMoWNbVN10-1-1 martensitic heat resistant steel for steam turbine blade, Journal of Materials Research and Technology 11 (2021) 2092–2105.
- [34] J. Wang, T. Liu, Y. Zhou, X. Xing, S. Liu, Y. Yang, Q. Yang, Effect of nitrogen alloying on the microstructure and abrasive impact wear resistance of Fe-Cr-C-Ti-Nb hardfacing alloy, Surf Coat Technol 309 (2017) 1072–1080.
- [35] X. Mao, P. Zhu, X. Sun, C. Xu, S. Huang, H. He, Z. Cheng, Effect of N on microstructure, nucleation mechanism and mechanical performance of (Ti, Nb) C particles in Fe-based composite coating via plasma spray welding, Surf Coat Technol 490 (2024) 131177.